

F3D-Gaus: Feed-forward 3D-aware Generation on ImageNet with Cycle-Consistent Gaussian Splatting

Yuxin Wang
HKUST

ywangom@connect.ust.hk

Qianyi Wu
Monash University

qianyi.wu@monash.edu

Dan Xu*
HKUST

danxu@cse.ust.hk

Abstract

This paper tackles the problem of generalizable 3D-aware generation from monocular datasets, e.g., ImageNet [10]. The key challenge of this task is learning a robust 3D-aware representation without multi-view or dynamic data, while ensuring consistent texture and geometry across different viewpoints. Although some baseline methods are capable of 3D-aware generation, the quality of the generated images still lags behind state-of-the-art 2D generation approaches, which excel in producing high-quality, detailed images. To address this severe limitation, we propose a novel feed-forward pipeline based on pixel-aligned Gaussian Splatting, coined as **F3D-Gaus**, which can produce more realistic and reliable 3D renderings from monocular inputs. In addition, we introduce a self-supervised cycle-consistent constraint to enforce cross-view consistency in the learned 3D representation. This training strategy naturally allows aggregation of multiple aligned Gaussian primitives and significantly alleviates the interpolation limitations inherent in single-view pixel-aligned Gaussian Splatting. Furthermore, we incorporate video model priors to perform geometry-aware refinement, enhancing the generation of fine details in wide-viewpoint scenarios and improving the model’s capability to capture intricate 3D textures. Extensive experiments demonstrate that our approach not only achieves high-quality, multi-view consistent 3D-aware generation from monocular datasets, but also significantly improves training and inference efficiency. Project Page: <https://w-ted.github.io/publications/F3D-Gaus>

1. Introduction

3D-aware generation from a single image has wide applications in virtual reality (VR), augmented reality (AR), gaming, and autonomous driving. Traditional methods for 3D-aware generation from a single image typically use voxels [9], point clouds [59] or meshes [13, 47] as 3D representations. However, in recent years, with the rise of NeRF [26]

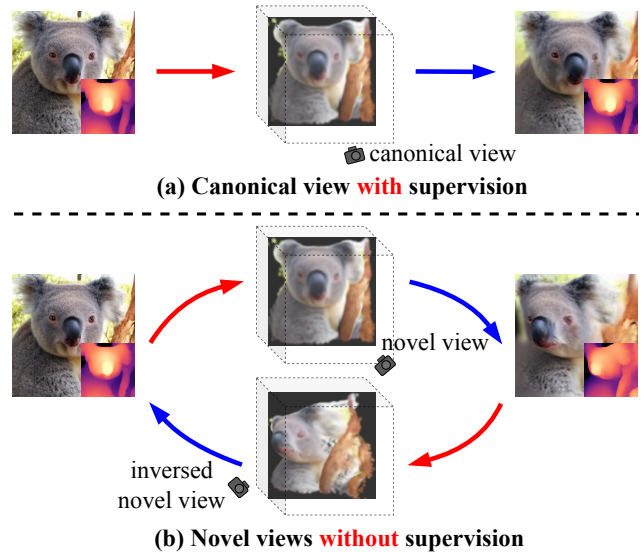


Figure 1. **Illustration of our motivation for cycle-consistent self-supervised training.** For monocular datasets: (a) supervision is naturally available for the canonical view. (b) For novel views, where supervision is absent, we use the rendered novel-view image as input to obtain its 3D representation. This 3D representation is then re-rendered from the canonical view, where supervision is available. **Red arrows** indicate feed-forward 3D representation prediction from a monocular image, while **blue arrows** represent the rendering processes from 3D representations at different specific viewpoints.

and 3D Gaussian Splatting (3DGS) [23] representations, methods based on NeRF [3, 39] and 3DGS [42, 44] have gained popularity due to their advantages in capturing fine details and handling complex lighting conditions.

In general, most recent 3D-aware generation methods rely on multi-view image supervision [19, 32, 35, 42, 44, 48, 65], fine-tuning on video data [12, 62], or optimization based on 2D/3D diffusion priors [43, 60]. However, compared to the availability of multi-view or high-resolution video data, monocular datasets are far more abundant and easier to collect. This is particularly advantageous because monocular data can be gathered from a wide range of sources, such as single-frame images from

the web or consumer-grade cameras, without requiring specialized equipment or controlled capture conditions. Our approach aims to explore the possibility of performing 3D-aware generation tasks using only monocular datasets, without the need for multi-view images or video data during training. This monocular setting also presents the potential for scaling up to larger datasets, which can lead to better generalization across a wider variety of scenes and objects. On the other hand, inference-time optimization methods [12, 43, 60] for 3D-aware generation often suffer from low efficiency and are impractical for real-world applications, especially in time-sensitive applications or environments with limited computational capacity. Therefore, to enhance accessibility and practicality, we propose a feed-forward framework based on pixel-aligned Gaussian Splatting that aims to directly infer 3D-aware representations in one single step, using only monocular datasets for training.

However, since monocular datasets only provide supervision for the frontal view, obtaining constraints for novel viewpoints is a key challenge. Previous methods trained on monocular datasets typically employ discriminators [39], semantic/geometry constraints [30], or iterative in-painting techniques [54] to generate plausible novel view images. We observe that while pixel-aligned Gaussian Splatting has advantages over previous approaches in terms of rendering realism, it struggles when the viewpoint changes significantly. Specifically, regions occluded in the original view are not easily interpolated with monocular Gaussian primitives to render plausible color and geometry in the new view. To address this issue, we introduced a self-supervised cycle constraint during training. This strategy ensures that the 3D representations from novel viewpoints are aligned with and complementary to those from the original viewpoint. By enforcing this cycle constraint, the model is naturally able to extrapolate across views by aggregating multiple representations to enhance the 3D capability during inference. Additionally, to correct any inconsistencies in geometry or textures caused by large viewpoint shifts, we incorporate a video in-painting model for refinement, resulting in a more reliable final output.

Throughout the development and evaluation of our approach, our 3D rendering results exhibit a remarkable level of realism, representing a substantial improvement over current challenging benchmarks. We also validate the robustness of our approach on a diverse set of datasets, including several single-category object-centric datasets and the more varied and extensive ImageNet [10] dataset, confirming its generalizability and practical applicability. In addition, our solution surpasses baseline methods in computational efficiency, significantly reducing both training and inference times without compromising performance.

Our work provides a holistic solution for realistic and efficient 3D-aware generation for monocular datasets, mark-

ing a significant advancement in 3D content generation. The summarized contribution of our paper is threefold:

- We pioneer 3D-aware generation using generalizable feed-forward Gaussian Splatting representation, achieving significant efficiency and favorable rendering quality on monocular datasets.
- We significantly advance the capability of pixel-aligned Gaussian Splatting representations by designing a self-supervised cycle training strategy specifically tailored for monocular datasets.
- We further mitigate the artifacts of 3D-aware representations caused by large viewpoint shifts by introducing geometry-aware video priors.

2. Related Works

2.1. Novel view synthesis for single input

With multi-view dataset. Novel view synthesis from a single image can be achieved through various methods. One straightforward strategy is to train or fine-tune models using multi-view or video data with camera information, which data naturally provides strong multi-view cues for 3D-aware generation. For instance, multi-view data is used to train models from scratch [19, 32, 42, 44, 67], or fine-tune pre-trained models for image generation [12, 18, 35, 48] or video generation [15, 25, 45, 52, 62] to achieve camera motion control. Another category of methods involves scene-specific optimization by leveraging the prior knowledge of 2D/3D diffusion models [17, 28, 43, 60]. However, scene-specific approaches are not generalizable, as they are tailored to individual objects or scenes.

With only monocular dataset. The approach most similar to ours trains a generalized model solely on monocular datasets and supports feed-forward predictions [3, 30, 31, 38, 54]. 3DGP [38] pioneered 3D-aware generation on ImageNet by training a model on 1,000 classes using a 3D-aware GAN for RGB-D prediction. It introduces a discriminator to distinguish real and generated images and employs a depth-adapter to refine unreliable depth predictions. Similarly, G3DR [30] uses a generalized tri-plane representation and semantic/perceptual losses for novel view rendering. Our method operates in a similar setting, but combines pixel-aligned Gaussian Splatting with a cycle-consistent training strategy, leading to more realistic renderings against the tri-plane approaches. In contrast, IVID [54] generates RGB-D in-painting pairs from ImageNet using a 2D diffusion model with iterative in-painting. However, it struggles to generalize to novel object categories, as it relies on matching input classes to ImageNet, inevitably limiting its adaptability to new categories.

2.2. 3D Gaussian Splatting

Recently, 3D Gaussian Splatting (3DGS) [23] stands as a leading representation for novel view synthesis, en-

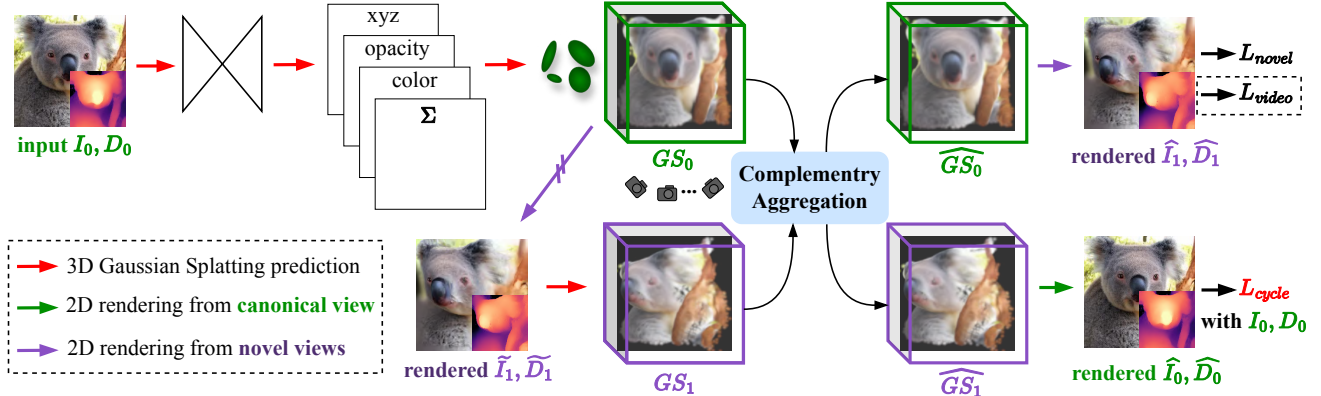


Figure 2. **Illustration of our overall framework.** Given a single RGB image I_0 and depth map D_0 , our model directly feeds them forward to output the pixel-aligned Gaussian Splatting representation GS_0 , which can be used for novel view synthesis. After obtaining the 3DGS representation, we render the image \hat{I}_1 and depth maps \hat{D}_1 for the novel view, and then output its corresponding 3DGS GS_1 . These two 3DGS representations are subsequently aggregated to produce the images for supervision. This novel self-supervised training strategy enforces cycle-consistent 3D representation learning across different views, allowing the generalized 3DGS representations to reinforce each other, thereby collaboratively enhancing the overall 3D representation capability.

abling real-time rendering with state-of-the-art visual quality. 3DGS models the 3D scene as a collection of learnable 3D Gaussian primitives with 3D coordinates, opacity, anisotropic covariance, and color features. Subsequent works apply 3DGS to downstream tasks such as scene understanding [2, 34, 64, 68, 70], scene editing [6, 46, 50, 57, 66], and surface reconstruction [5, 20, 24, 51, 53, 55, 63]. However, 3DGS was originally designed for scene-specific novel view synthesis. Recent works introduced generalizable models for predicting 3DGS from single or multiple images [4, 7, 8, 40–42, 44]. For example, Splatter-Image [42] pioneered pixel-aligned 3DGS prediction from RGB images, enabling fast feed-forward training and inference. LGM [44] combines pre-trained multi-view image generation models with an image-to-3DGS model, achieving object-level 3DGS inference from a single image. Flash3D [41] integrates a depth estimation model for scene-level 3DGS prediction from a single image. While these methods allow feed-forward inference from a single image to 3DGS, they still rely on multi-view data for training or use multi-view image generation models as priors. In contrast, our approach focuses on generalized 3DGS prediction without requiring multi-view images for training.

3. The Proposed Framework: F3D-Gaus

Given a dataset of images and their corresponding monocular depth maps, represented as $\{(I_i, D_i) | i = 0, \dots, N\}$, we aim to train a generalized model that takes a single RGB-D input and outputs the associated 3DGS representation in a feed-forward manner. This representation can then be utilized for novel view synthesis. The monocular depth maps D_i can be easily obtained using monocular depth estimation models [22, 56, 58].

As shown in Fig. 2, we use a U-Net-based generalized

3DGS model as the backbone. Given an input image I_0 and its depth map D_0 , the model predicts a pixel-aligned 3DGS representation, which can render images and depth maps from arbitrary viewpoints [63]. The details of the generalized 3DGS model are provided in Sec. 3.1. As shown in Fig. 1, the rendered outputs can be supervised in the canonical view but the monocular dataset lacks supervision for novel views. We propose a cycle-consistent self-supervised training strategy in Sec. 3.2 to address this. Additionally, our geometry-guided refinement method introduced in Sec. 3.3 further identifies and refines artifacts.

3.1. Preliminary

3D Gaussian Splatting. Each Gaussian primitive is characterized by its 3D coordinates μ , color features c , opacity, scale matrix S , and rotation matrix R . With these attributes, the Gaussians are defined by the covariance matrix $\Sigma = RSS^T R^T$ centered at point μ :

$$G(\mathbf{x}) = \exp^{-\frac{1}{2}(\mathbf{x}-\mu)^T \Sigma^{-1}(\mathbf{x}-\mu)}. \quad (1)$$

The covariance matrix is projected onto the 2D plane following [71], allowing us to compute the projected Gaussian and apply alpha-blending to obtain the final color on the image plane:

$$\hat{I} = \sum_{k=1}^K c_k \alpha_k \Pi_{j=1}^{k-1} (1 - \alpha_j), \quad (2)$$

where K is the number of sampling points along the ray and α is derived from the projected Gaussian of $G(\mathbf{x})$ and its corresponding opacity. More details can be found in [23].

Pixel-aligned 3DGS. Splatter-Image [42] introduces a framework for predicting pixel-aligned 3DGS from RGB images. Given an input image I_0 , the model predicts Gaussian attribute maps, including 3D coordinates, opacity, color

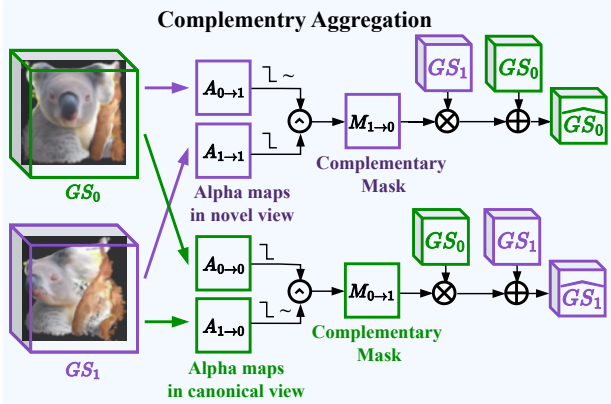


Figure 3. **Illustration of complementary aggregation in the proposed cycle-consistency self-supervised strategy.** We guide complementary aggregation by leveraging the differences between the alpha maps of the two 3DGS from different viewpoints.

features, scale, and rotation. For an input of size $H \times W$, the output attribute maps have the same spatial size, corresponding to $n = H \times W$ Gaussian primitives. The scale and rotation define the covariance matrix. Together with 3D coordinates, opacity, and color features, the 3DGS can render images and depth maps from arbitrary viewpoints.

As shown in Fig. 2, we use a similar U-Net-based generalized 3DGS model as the backbone. The final 3D coordinates of the 3DGS are computed by adding the input depth D_0 to the predicted offset.

3.2. Cycle-consistent Self-supervised Strategy

The lack of novel view supervision motivates us to propose a cycle-consistent self-supervised strategy in this section. It aims to ensure the multi-view consistency of the predicted 3DGS. It has two key components: complementary aggregation and cycle supervision. The details are given below.

Canonical view reconstruction. We assume each image in the monocular dataset is captured from a canonical view. During training, we pass RGB-D input (I_0, D_0) through the model to obtain the output GS_0 . We then randomly sample camera views to render the scene from either the canonical view, represented as $view_0$, or a randomly selected novel view $view_1$. If the canonical view is rendered, as shown in Fig. 1 (a), a reconstruction loss is applied directly to the predicted image \hat{I}_0 and depth map \hat{D}_0 , effectively performing RGB-D image reconstruction.

$$\mathcal{L}_{\text{recon}} = \|\hat{I}_0 - I_0\|_1 + \|\hat{D}_0 - D_0\|_1 \quad (3)$$

The backpropagated gradients update the parameters of our U-Net backbone via the 3DGS attribute maps.

Complementary aggregation. The idea behind complementary aggregation is as follows: our method can predict the canonical GS_0 from the input I_0 and D_0 , we assume that if we had a side-view image of the same object (even though

the dataset lacks ground truth for side views, we can render one from GS_0 , denoted as \hat{I}_1 and \hat{D}_1 in Fig. 2), we could also obtain a novel view GS_1 . We aim to enforce multi-view consistency between the rendered \hat{I}_1, \hat{D}_1 and the original I_0, D_0 , which implies that GS_0 and GS_1 should also be multi-view consistent. Another intuition is that, GS_0 and GS_1 are 3D representations from two different views but they represent the same scene, they should also be complementary. Thus, we designed complementary aggregation to ensure that GS_0 and GS_1 are both multi-view consistent and complementary.

As shown in Fig. 3, after obtaining GS_0 and GS_1 , we apply an aggregation strategy to update both 3DGSs. Specifically, we first render the alpha maps \hat{A} for both the $view_0$ and the $view_1$ from the two 3DGS representations.

$$\hat{A} = \sum_{k=1}^K \alpha_k \prod_{j=1}^{k-1} (1 - \alpha_j), \quad (4)$$

α and K have the same meaning as Equ. 2. In Fig. 3, $A_{i \rightarrow j}$ represents the alpha map rendered from GS_i in view j . We binarize (\lfloor) the alpha maps to detect invisible region in GS_i at specific locations in view j . Using logical operations, we then generate two complementary masks:

$$\begin{aligned} M_{1 \rightarrow 0} &= \neg(A_{0 \rightarrow 1} < \tau) \wedge (A_{1 \rightarrow 1} < \tau) \\ M_{0 \rightarrow 1} &= (A_{0 \rightarrow 0} < \tau) \wedge \neg(A_{1 \rightarrow 1} < \tau) \end{aligned} \quad (5)$$

We set $\tau = 0.5$, where \neg represents logical negation, and \wedge represents the logical and. $M_{1 \rightarrow 0}$ identifies the locations in $view_1$ where GS_0 has holes but GS_1 has valid values, indicating the specific primitives in GS_1 that can contribute to GS_0 . These complementary masks are then used to update GS_0 and GS_1 , as shown in Fig. 3.

$$\begin{aligned} \hat{GS}_0 &= \text{Concat}(GS_0, GS_1[M_{1 \rightarrow 0}]) \\ \hat{GS}_1 &= \text{Concat}(GS_1, GS_0[M_{0 \rightarrow 1}]) \end{aligned} \quad (6)$$

In the equations above, $[M_{i \rightarrow j}]$ uses the complementary mask to select the corresponding pixel-aligned primitives. The function $\text{Concat}(*, *)$ combines two sets of 3DGS primitives into a new set.

Cycle supervision. As shown in Fig. 2, after obtaining the updated \hat{GS}_0 and \hat{GS}_1 , we render \hat{I}_1, \hat{D}_1 from $view_1$ and \hat{I}_0, \hat{D}_0 from $view_0$, respectively. Note that the rendered views are opposite to the source input view of the GS representations. This augmentation is designed to maximize the use of supervision. For \hat{I}_0 and \hat{D}_0 , we use the original I_0 and D_0 for supervision, referred to as cycle consistency loss:

$$\mathcal{L}_{\text{cycle}} = \|\hat{I}_0 - I_0\|_1 + \|\hat{D}_0 - D_0\|_1 \quad (7)$$

The cycle loss $\mathcal{L}_{\text{cycle}}$ in Equ. 7 looks the same as the reconstruction loss in Equ. 3, but they correspond to sampled canonical and novel views, respectively. The predictions of \hat{I}_0 and \hat{D}_0 differ in each case. Due to our complementary

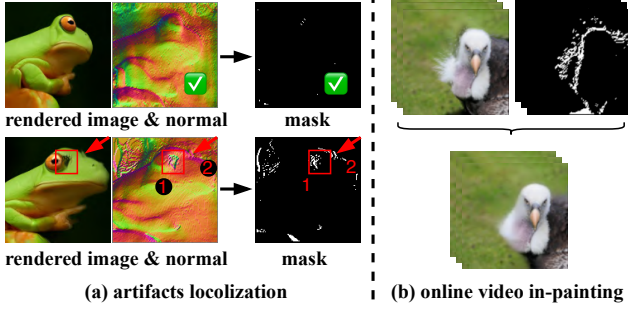


Figure 4. **Illustration of geometry-guided texture refinement.** (a) illustrates artifact localization in novel views, while (b) shows geometry mask-guided sequence in-painting.

aggregation design, the gradients from $\mathcal{L}_{\text{cycle}}$ backpropagate through both GS_0 and GS_1 . We block gradient propagating to GS_0 via \hat{I}_1 and \hat{D}_1 , as we found that allowing it hinders the learning process.

Overall losses. For \hat{I}_1 and \hat{D}_1 , we apply perceptual loss [21] and CLIP losses [29] following [30]. In addition, we use photometric loss to the novel views by warping textures from the frontal view with depth D_0 .

$$\begin{aligned}\mathcal{L}_{\text{perp}} &= \sum_l \left\| \phi_l(\hat{I}_1) - \phi_l(I_0) \right\|_2 \\ \mathcal{L}_{\text{CLIP}} &= \left\| \phi_{\text{CLIP}}(\hat{I}_1) - \phi_{\text{CLIP}}(I_0) \right\|_1 \\ \mathcal{L}_{\text{photo}} &= \left\| I_0(x_i) - \hat{I}_1(P(D_0(x_i), \pi, T_{0 \rightarrow 1})) \right\|_1\end{aligned}\quad (8)$$

ϕ_l represents the feature extractor from the first l layers of a perceptual model, while ϕ_{CLIP} refers to the CLIP feature extractor. $\hat{I}_1(P(D_0(x_i), \pi, T_{0 \rightarrow 1}))$ denotes the RGB value of the reprojected predicted image \hat{I}_1 at pixel x_i , where π is the camera intrinsic matrix, $T_{0 \rightarrow 1}$ is the extrinsic matrix, P is the projection function transforming from view₀ to view₁. We then define the losses for the novel view as follows:

$$\mathcal{L}_{\text{novel}} = \mathcal{L}_{\text{photo}} + \lambda_{\text{perp}} \mathcal{L}_{\text{perp}} + \lambda_{\text{CLIP}} \mathcal{L}_{\text{CLIP}} \quad (9)$$

Note that novel loss $\mathcal{L}_{\text{novel}}$ defined in Equ. 9 is not part of our cycle-consistent training strategy, but rather a component of our baseline method. Even in the baseline method mentioned in the ablation study in Sec. 4.3, the novel loss is also applied (to \tilde{I}_1 and \tilde{D}_1 at that time). In addition to the above losses, we apply a regularization loss to enforce smoothness in the rendered depth.

$$\mathcal{L}_{\text{reg}} = L_{\text{tv}}(\hat{D}) \quad (10)$$

The overall training loss is shown below, where λ represents the weight of each loss term.

$$\mathcal{L}_{\text{total}} = \begin{cases} \mathcal{L}_{\text{recon}} + \lambda_{\text{reg}} \mathcal{L}_{\text{reg}}, & \text{for canonical view,} \\ \mathcal{L}_{\text{cycle}} + \lambda_{\text{reg}} \mathcal{L}_{\text{reg}} \\ \quad + \lambda_{\text{novel}} \mathcal{L}_{\text{novel}} & \text{for novel views.} \end{cases} \quad (11)$$

Inference-time aggregation. During training, we use a

cycle-consistent training strategy by aggregating GS representations from two views and aligning them via cycle supervision. This naturally extends to multi-view aggregation during inference, enhancing representational capacity. At inference time, given inputs I_0 and D_0 , we first obtain GS_0 . We then render eight images from GS_0 along a spiral trajectory. Next, we run another inference step to obtain eight distinct GS_1 representations, which are concatenated with GS_0 to form the final GS representation.

3.3. Geometry-guided Texture Refinement

We found that although our cycle-consistent self-supervised strategy improves 3D representations in novel views, there are still artifacts near edges with significant viewpoint changes. To address this, we introduce a fixed video in-painting model [69] in the second training stage for artifact localization and additional refinement.

Artifacts localization using normal map. When rendering novel view images from GS_0 , we also render the alpha map and calculate the normal map from the depth [63]. We found that alpha and normal maps effectively help identify artifacts. Specifically, if the alpha value is low and the angle between the normal and viewing direction is small, it is likely an artifact. This can be formalized as follows:

$$M_{\text{artifact}} = (\hat{A} < \tau) \wedge (\cos^{-1}(\hat{N} \cdot \mathbf{v}) < \tau_{\theta}) \quad (12)$$

where \hat{N} is the normal map calculated from depth map, \mathbf{v} is the viewing direction, and τ and τ_{θ} are small thresholds.

The rationale for using the normal map to detect artifacts is that poorly learned GS primitives in novel views tend to produce surface normals nearly parallel to the viewing direction. As shown in Fig. 4, we use the normal map to identify these artifacts. For small novel view changes, the rendered image and normals remain reasonable, and the corresponding mask is mostly zero. However, with larger view changes, holes appear near the frog’s eyes due to a lack of Gaussian primitives, as indicated by very low alpha values. Additionally, redundant artifacts emerge on the top of the frog’s head, visible in the rendered normal map. The mask on the right effectively highlights these artifact locations, highlighted by red arrows and boxes.

Online sequence in-painting. After localizing the artifacts, we uniformly sample 16 views between view₀ and view₁, and render both the images \hat{I}^m and depth maps \hat{D}^m for these views from GS_0 . We then apply the video in-painting model [69], guided by masks generated from the alpha and normal maps, to fill in the missing regions in these 16 frames. The in-painted textures are subsequently used to supervise the rendered images in sequence. The in-painting process can be formulated as:

$$(I_{\text{in}}^1, \dots, I_{\text{in}}^{16}) = \mathcal{F}_{\text{in}} \left((\hat{I}^1, M^1), \dots, (\hat{I}^{16}, M^{16}) \right) \quad (13)$$

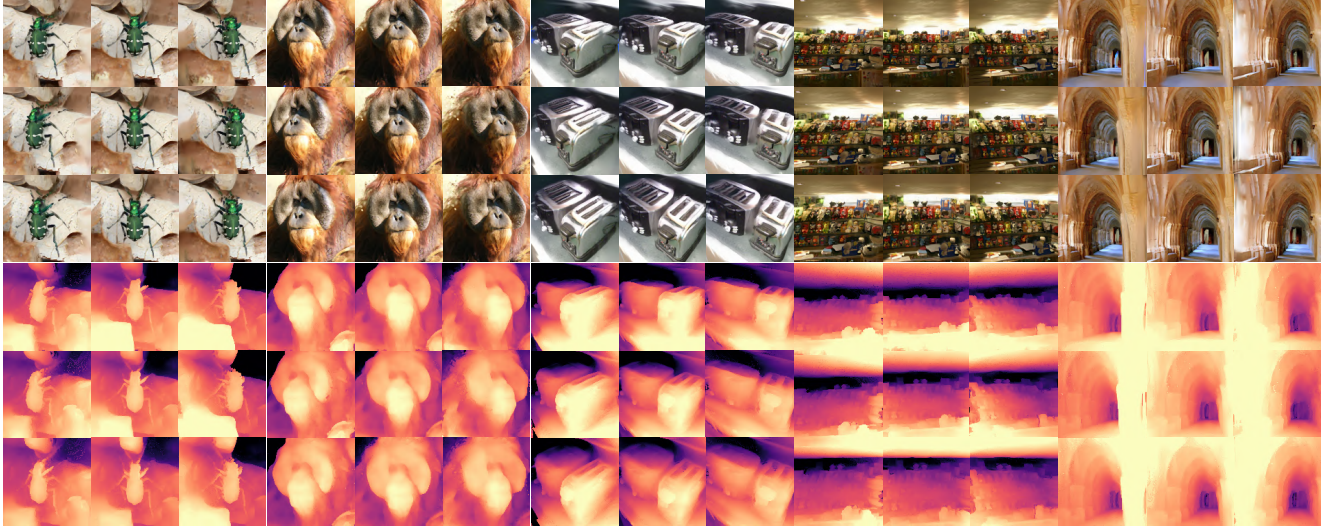


Figure 5. **Qualitative visualization of rendered images and depth maps on the ImageNet dataset.** Our method can generate novel view images along with corresponding depth maps for input images across various categories.

where I_{in}^m represents the in-painted image for the m -th frame, \hat{I}^m is the rendered image, and M^m is the mask generated from Equ. 12. Fig. 4 (b) shows one view of the in-painted results. Then, the corresponding video in-painting loss is defined as:

$$L_{\text{video}} = \sum_{m=1}^{16} \left\| M^m \cdot (\hat{I}^m - I_{in}^m) \right\|_1 \quad (14)$$

The in-painting process is performed online, and this video loss L_{video} is added to L_{total} to fine-tune the pre-trained model with a smaller learning rate.

4. Experiments

4.1. Experimental Setup

Dataset. We conducted experiments on the ImageNet dataset [10], Dogs [27], SDIP Elephants [27], and LSUN Horses [61], following previous methods. ImageNet contains 1000 categories of images, while the other three datasets consist of single-class images. For a fair comparison, we utilize pseudo-ground-truth depth from LeReS [58], though our approach can be extended to other state-of-the-art depth estimation methods. We follow the 3DGP [38] settings for ImageNet, training on a filtered subset (420K images) and evaluating the full training set (1.2M images). Most of our experiments are conducted on ImageNet.

Metrics. For the generated images, we compute Fréchet Inception Distance (FID) [16] and Inception Score (IS) on the full ImageNet training set. For the predicted depth maps, we calculate the normalized L2 distance between the predicted depth and pseudo ground-truth depth. Additionally, we compute the Non-Flatness Score (NFS) [38], a no-reference depth quality metric that evaluates the continuity by analyzing the histogram distribution of the depth map.

Method	Synthesis	FID ↓	IS ↑
BigGAN [1]	2D	8.7	142.3
StyleGAN-XL [33]	2D	2.3	265.1
ADM [11]	2D	4.6	186.7
EG3D [3]	3D-aware	25.6	57.3
StyleNeRF [14]	3D-aware	56.5	21.8
3DPhoto [36]	3D-aware	116.6	9.5
EpiGRAF [37]	3D	58.2	20.4
3DGP [38]	3D	19.7	124.8
VQ3D [31]	3D	16.8	n/a
G3DR [30]	3D	13.1	151.7
Our F3D-Gaus	3D	1.6	308.6

Table 1. **Fidelity comparison on ImageNet 256².** Our **F3D-Gaus** surpasses all listed state-of-the-art 3D generation methods in both FID and IS metrics, achieving results comparable to those of 2D generation methods.

4.2. Main Results

Quantitative results. Fig. 5, Tab. 1, Tab. 2 and Tab. 3 present the qualitative and quantitative results of our method on the ImageNet dataset. The metrics in Tab. 1 and Tab. 2 are computed on the full training set at a resolution of 256, where our method outperforms all baselines across all metrics. In Tab. 1, single-image reconstruction methods are grouped into 2D and 3D approaches. Generally, 2D methods achieve higher scores than 3D methods, with FID values typically below 10. Among 3D methods, our approach significantly outperforms the others, achieving an FID 1.6 and an IS 308.6, reaching a performance level comparable to 2D methods. This indicates that our generated images are closer to real images in distribution. Similarly, in Tab. 2, our method achieves the best results, demonstrating superior performance in rendering depth maps. Tab. 3 shows our method significantly outperforms the baseline in image

Method	Depth accuracy ↓	NFS ↑
3DGP [38]	0.47	18.5
IVID [54]	1.23	19.2
G3DR [30]	0.39	36.5
Our F3D-Gaus	0.16	40.4

Table 2. **Geometry comparison between our method and three state-of-the-art methods on ImageNet 256².** Our F3D-Gaus outperforms all three methods in both depth accuracy and NFS.

Method	FID ↓	IS ↑
IVID [54] 128x	14.1	61.4
G3DR [30] 128x	13.0	136.4
Our F3D-Gaus 128x	1.2	202.8

Table 3. **Fidelity comparison with two state-of-the-art methods on ImageNet 128².** Our F3D-Gaus outperforms both IVID and G3DR at this resolution.

fidelity at a resolution of 128.

Qualitative results. Fig. 5 showcases the 3DGS renderings from our model in both canonical and novel views across a wide range of categories. These categories include slender-legged insects, animals, household items, detailed objects, and large structures, demonstrating its ability to handle diverse data and produce high-quality results. Fig. 6 provides additional qualitative results on three single-class datasets, further illustrating the effectiveness of our approach. In addition to accurately reconstructing the original view, our method generates plausible and coherent novel views.

Out-of-domain samples. Fig. 8 shows the results of our method on more complex, scene-level inputs that fall outside the scope of the ImageNet dataset. These out-of-domain samples, which include intricate indoor scenes and multi-object environments, introduce a significantly higher complexity compared to the object-centric images in ImageNet. Despite the challenge, our model trained on ImageNet at a resolution of 256² successfully produces high-quality novel view renderings, including images, depth maps, and normal maps across different viewpoints, demonstrating its impressive generalization capabilities.

4.3. Ablation Study

Fig. 7 and Fig. 9 demonstrate the effectiveness of our proposed modules quantitatively and qualitatively.

Overall analysis. Fig. 7 illustrates how different components of our method affect the metrics as the rendered view angle increases. For efficiency, the metrics in Fig. 7 are computed on a subset of ImageNet at a resolution of 128. Specifically, the three subplots in Fig. 7 correspond to three metrics: IS, FID, and NFS. Each subplot contains three curves, representing different variants of our framework. The green line represents the baseline, which uses only the pixel-aligned representation without cycle-consistent training or second-stage refinement. In this variant, there is

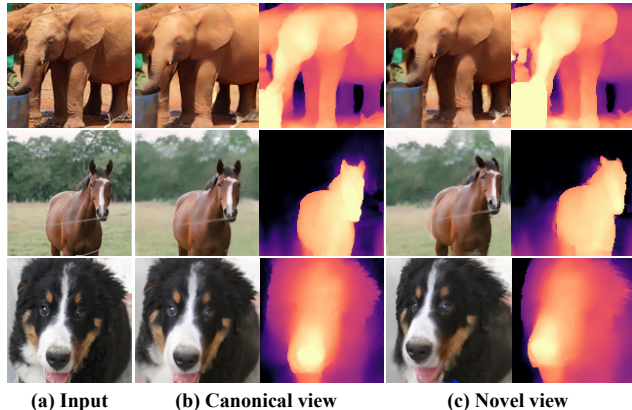


Figure 6. **Qualitative visualization of rendered images and depth maps** on the SDIP Elephants [27], LSUN Horses [61], and Dogs [27] datasets.

no complementary aggregation, and $\mathcal{L}_{\text{cycle}}$ is removed from Equ. 11, and $\mathcal{L}_{\text{novel}}$ is applied to \tilde{I}_1 and \tilde{D}_1 , rather than \hat{I}_1 and \hat{D}_1 . The blue line represents the model with cycle-consistent training, while the red line represents the full model, which includes both cycle-consistent training and second-stage refinement.

Pixel-aligned 3DGS. From the three subplots in Fig. 7, we observe that at a 0-degree angle, the differences between the three variants are minimal, with the baseline (green line) even achieving the highest IS and NFS. This suggests that the generalized 3DGS representation alone can produce high-quality frontal view reconstructions. However, the baseline’s performance degrades significantly as the yaw angle increases. For rendering angles sampled between $[-30^\circ, 30^\circ]$, the baseline’s IS drops to 218.0, FID rises to 11.3, and NFS declines sharply. This indicates that, while the baseline performs well for frontal views, it struggles to represent texture and geometry effectively in novel views.

Cycle-consistent training. In contrast, the blue line, which includes cycle-consistent training, shows more stable performance as the viewing angle increases, with only a slight decline in metrics. This demonstrates that the cycle-consistent training helps our method better leverage monocular datasets to learn 3D perception capabilities.

Fig. 9 illustrates the effect of our cycle-consistent training strategy on the generated novel view results. For two input images, the right side shows the rendered images, depth maps, and normal maps from novel views. Without the cycle-consistent training strategy, the novel views exhibit noticeable ghosting artifacts. For example, for input 1, the novel view of the mug shows a faint outline of an additional edge, and for input 2, the head appears to have multiple overlapping layers. These artifacts suggest that the 3DGS representations derived from different viewpoints are not well-aligned, which contradicts our goal of learning a consistent 3D-aware representation. However,

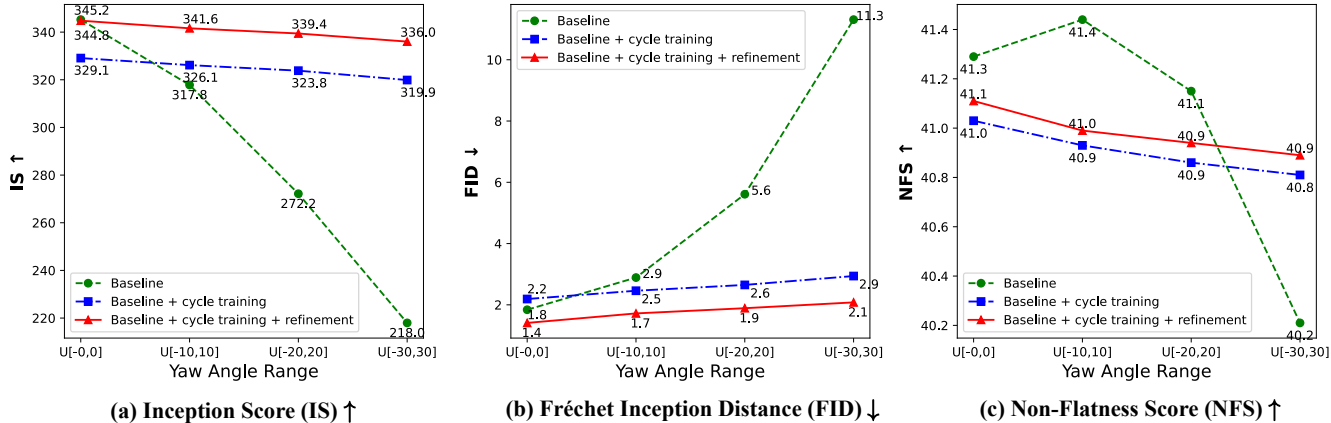


Figure 7. Performance comparison of three 128^2 models across varying yaw angle ranges. The FID, IS, and NFS metrics are evaluated on the filtered subset of ImageNet. The x-axis represents the yaw angle ranges, while the y-axis denotes the corresponding metric values.

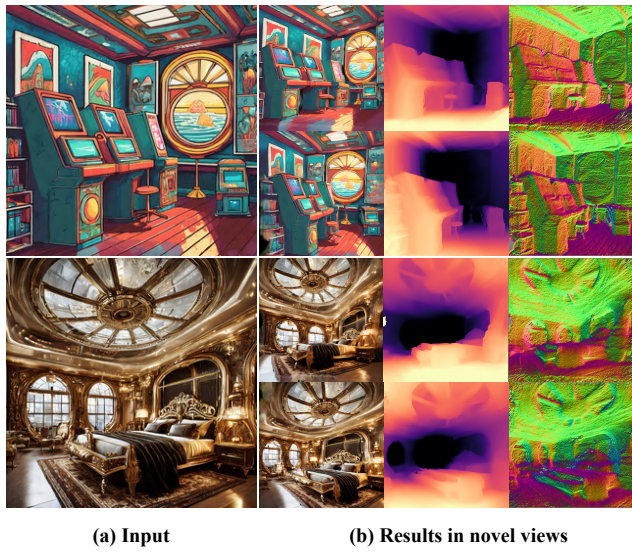


Figure 8. Results on two complex indoor scene images outside the ImageNet dataset. The rendered novel view images, along with their corresponding depth and normal maps, effectively demonstrate the generalization capability of our model.

after applying the cycle-consistent training strategy, the rendered results become much more coherent, and the ghosting artifacts are noticeably fixed. This demonstrates that the cycle-consistent strategy helps produce more consistent and aligned 3D representations across different views.

Geometry-guided refinement. In Fig. 7, comparing the blue line and the red line in three subplots, we can find that when we add the second-stage geometry-guided refinement, the red line shows obvious improvements, achieving the best results among all the three metrics. This suggests that the second-stage refinement further enhances the model’s image and geometry rendering. Additionally, the fine-tuning refinement does not affect the multi-view consistency established by the cycle training. The red line shows only minor degradation as the yaw angle increases. This in-

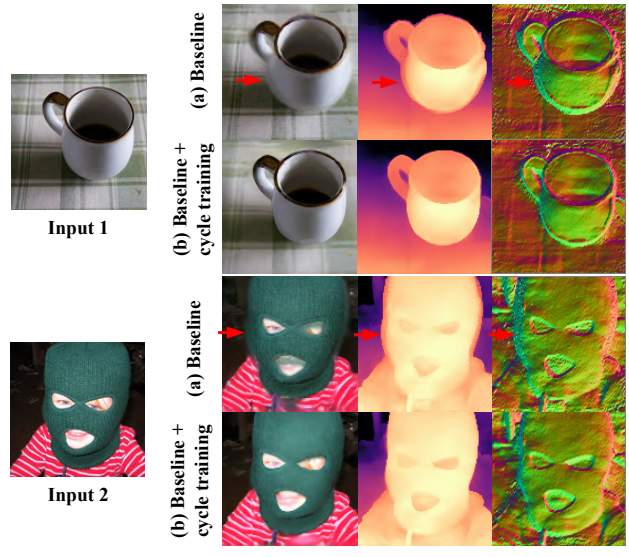


Figure 9. Demonstration of the effectiveness of cycle-consistent self-supervised training. The comparison between (a) and (b) clearly highlights that our cycle-consistent training strategy significantly mitigates ghosting artifacts.

dicates that the second-stage refinement further strengthens the model’s ability to maintain high-quality results, even as the viewing angle becomes more challenging.

5. Conclusion

We are the first to apply pixel-aligned Gaussian Splatting representations to generalizable 3D-aware generation on monocular datasets. In the absence of multi-view or dynamic data, we propose a self-supervised cycle training strategy that effectively merges multiple geometry-aligned 3D representations for better 3D-aware capability. We also incorporate video-based priors for geometry-aware detail refinement, particularly in wide-angle views. Experimental results demonstrate that our method outperforms previous baselines in both effectiveness and efficiency.

References

- [1] Karen Simonyan Andrew Brock, Jeff Donahue. Large scale gan training for high fidelity natural image synthesis. *ICLR*, 2019. 6
- [2] Yang Cao, Yuanliang Jv, and Dan Xu. 3dgs-det: Empower 3d gaussian splatting with boundary guidance and box-focused sampling for 3d object detection. *arXiv preprint arXiv:2410.01647*, 2024. 3
- [3] Eric R Chan, Connor Z Lin, Matthew A Chan, Koki Nagano, Boxiao Pan, Shalini De Mello, Orazio Gallo, Leonidas J Guibas, Jonathan Tremblay, Sameh Khamis, et al. Efficient geometry-aware 3d generative adversarial networks. In *CVPR*, 2022. 1, 2, 6
- [4] David Charatan, Sizhe Lester Li, Andrea Tagliasacchi, and Vincent Sitzmann. pixelsplat: 3d gaussian splats from image pairs for scalable generalizable 3d reconstruction. In *CVPR*, 2024. 3
- [5] Danpeng Chen, Hai Li, Weicai Ye, Yifan Wang, Weijian Xie, Shangjin Zhai, Nan Wang, Haomin Liu, Hujun Bao, and Guofeng Zhang. Pgsr: Planar-based gaussian splatting for efficient and high-fidelity surface reconstruction. *arxiv preprint arxiv:2406.06521*, 2024. 3
- [6] Yiwen Chen, Zilong Chen, Chi Zhang, Feng Wang, Xiaofeng Yang, Yikai Wang, Zhongang Cai, Lei Yang, Huaping Liu, and Guosheng Lin. Gaussianeditor: Swift and controllable 3d editing with gaussian splatting. In *CVPR*, 2024. 3
- [7] Yuedong Chen, Chuanxia Zheng, Haofei Xu, Bohan Zhuang, Andrea Vedaldi, Tat-Jen Cham, and Jianfei Cai. Mvsplat360: Feed-forward 360 scene synthesis from sparse views. *NeurIPS*, 2024. 3
- [8] Yuedong Chen, Haofei Xu, Chuanxia Zheng, Bohan Zhuang, Marc Pollefeys, Andreas Geiger, Tat-Jen Cham, and Jianfei Cai. Mvsplat: Efficient 3d gaussian splatting from sparse multi-view images. In *ECCV*, 2025. 3
- [9] Christopher B Choy, Danfei Xu, JunYoung Gwak, Kevin Chen, and Silvio Savarese. 3d-r2n2: A unified approach for single and multi-view 3d object reconstruction. In *ECCV*, 2016. 1
- [10] Jia Deng, Wei Dong, Richard Socher, Li-Jia Li, Kai Li, and Li Fei-Fei. Imagenet: A large-scale hierarchical image database. In *CVPR*, 2009. 1, 2, 6
- [11] Prafulla Dhariwal and Alexander Nichol. Diffusion models beat gans on image synthesis. *NeurIPS*, 2021. 6
- [12] Ruiqi Gao, Aleksander Holynski, Philipp Henzler, Arthur Brussee, Ricardo Martin-Brualla, Pratul Srinivasan, Jonathan T Barron, and Ben Poole. Cat3d: Create anything in 3d with multi-view diffusion models. *arXiv preprint arXiv:2405.10314*, 2024. 1, 2
- [13] Georgia Gkioxari, Jitendra Malik, and Justin Johnson. Mesh r-cnn. In *ICCV*, 2019. 1
- [14] Jiatao Gu, Lingjie Liu, Peng Wang, and Christian Theobalt. Stylenerf: A style-based 3d-aware generator for high-resolution image synthesis. *ICLR*, 2022. 6
- [15] Yuwei Guo, Ceyuan Yang, Anyi Rao, Zhengyang Liang, Yaohui Wang, Yu Qiao, Maneesh Agrawala, Dahua Lin, and Bo Dai. Animatediff: Animate your personalized text-to-image diffusion models without specific tuning. *ICLR*, 2024. 2
- [16] Martin Heusel, Hubert Ramsauer, Thomas Unterthiner, Bernhard Nessler, and Sepp Hochreiter. Gans trained by a two time-scale update rule converge to a local nash equilibrium. *NeurIPS*, 2017. 6
- [17] Lukas Höllein, Ang Cao, Andrew Owens, Justin Johnson, and Matthias Nießner. Text2room: Extracting textured 3d meshes from 2d text-to-image models. In *ICCV*, 2023. 2
- [18] Lukas Höllein, Aljaž Božič, Norman Müller, David Novotny, Hung-Yu Tseng, Christian Richardt, Michael Zollhöfer, and Matthias Nießner. Viewdiff: 3d-consistent image generation with text-to-image models. In *CVPR*, 2024. 2
- [19] Yicong Hong, Kai Zhang, Jiuxiang Gu, Sai Bi, Yang Zhou, Difan Liu, Feng Liu, Kalyan Sunkavalli, Trung Bui, and Hao Tan. Lrm: Large reconstruction model for single image to 3d. *arXiv preprint arXiv:2311.04400*, 2023. 1, 2
- [20] Binbin Huang, Zehao Yu, Anpei Chen, Andreas Geiger, and Shenghua Gao. 2d gaussian splatting for geometrically accurate radiance fields. In *SIGGRAPH*, 2024. 3
- [21] Justin Johnson, Alexandre Alahi, and Li Fei-Fei. Perceptual losses for real-time style transfer and super-resolution. In *ECCV*, 2016. 5
- [22] Bingxin Ke, Anton Obukhov, Shengyu Huang, Nando Metzger, Rodrigo Caye Daudt, and Konrad Schindler. Repurposing diffusion-based image generators for monocular depth estimation. In *CVPR*, 2024. 3
- [23] Bernhard Kerbl, Georgios Kopanas, Thomas Leimkühler, and George Drettakis. 3d gaussian splatting for real-time radiance field rendering. *ToG*, 2023. 1, 2, 3
- [24] Xiaoyang Lyu, Yang-Tian Sun, Yi-Hua Huang, Xiuzhe Wu, Ziyi Yang, Yilun Chen, Jiangmiao Pang, and Xiaojuan Qi. 3dgsr: Implicit surface reconstruction with 3d gaussian splatting. *arXiv preprint arXiv:2404.00409*, 2024. 3
- [25] Luke Melas-Kyriazi, Iro Laina, Christian Rupprecht, Natalia Neverova, Andrea Vedaldi, Oran Gafni, and Filippos Kokkinos. Im-3d: Iterative multiview diffu-

- sion and reconstruction for high-quality 3d generation. *ICML*, 2024. 2
- [26] Ben Mildenhall, Pratul P Srinivasan, Matthew Tancik, Jonathan T Barron, Ravi Ramamoorthi, and Ren Ng. Nerf: Representing scenes as neural radiance fields for view synthesis. *Communications of the ACM*, 2021. 1
- [27] Ron Mokady, Omer Tov, Michal Yarom, Oran Lang, Inbar Mosseri, Tali Dekel, Daniel Cohen-Or, and Michal Irani. Self-distilled stylegan: Towards generation from internet photos. In *SIGGRAPH*, 2022. 6, 7, 2
- [28] Guocheng Qian, Jinjie Mai, Abdullah Hamdi, Jian Ren, Aliaksandr Siarohin, Bing Li, Hsin-Ying Lee, Ivan Skorokhodov, Peter Wonka, Sergey Tulyakov, and Bernard Ghanem. Magic123: One image to high-quality 3d object generation using both 2d and 3d diffusion priors. In *ICLR*, 2024. 2
- [29] Alec Radford, Jong Wook Kim, Chris Hallacy, Aditya Ramesh, Gabriel Goh, Sandhini Agarwal, Girish Sastry, Amanda Askell, Pamela Mishkin, Jack Clark, et al. Learning transferable visual models from natural language supervision. In *ICML*, 2021. 5
- [30] Pradyumna Reddy, Ismail Elezi, and Jiankang Deng. G3dr: Generative 3d reconstruction in imagenet. In *CVPR*, 2024. 2, 5, 6, 7
- [31] Kyle Sargent, Jing Yu Koh, Han Zhang, Huiwen Chang, Charles Herrmann, Pratul Srinivasan, Jiajun Wu, and Deqing Sun. Vq3d: Learning a 3d-aware generative model on imagenet. In *ICCV*, 2023. 2, 6
- [32] Kyle Sargent, Zizhang Li, Tanmay Shah, Charles Herrmann, Hong-Xing Yu, Yunzhi Zhang, Eric Ryan Chan, Dmitry Lagun, Li Fei-Fei, Deqing Sun, and Jiajun Wu. ZeroNVS: Zero-shot 360-degree view synthesis from a single real image. *CVPR*, 2024. 1, 2
- [33] Axel Sauer, Katja Schwarz, and Andreas Geiger. Stylegan-xl: Scaling stylegan to large diverse datasets. In *SIGGRAPH*, 2022. 6
- [34] Jin-Chuan Shi, Miao Wang, Hao-Bin Duan, and Shao-Hua Guan. Language embedded 3d gaussians for open-vocabulary scene understanding. In *CVPR*, 2024. 3
- [35] Yichun Shi, Peng Wang, Jianglong Ye, Long Mai, Kejie Li, and Xiao Yang. Mvdream: Multi-view diffusion for 3d generation. *arXiv:2308.16512*, 2023. 1, 2
- [36] Meng-Li Shih, Shih-Yang Su, Johannes Kopf, and Jia-Bin Huang. 3d photography using context-aware layered depth inpainting. In *CVPR*, 2020. 6
- [37] Ivan Skorokhodov, Sergey Tulyakov, Yiqun Wang, and Peter Wonka. Epigraf: Rethinking training of 3d gans. *NeurIPS*, 2022. 6, 2
- [38] Ivan Skorokhodov, Aliaksandr Siarohin, Yinghao Xu, Jian Ren, Hsin-Ying Lee, Peter Wonka, and Sergey Tulyakov. 3d generation on imagenet. In *ICLR*, 2023. 2, 6, 7
- [39] Ivan Skorokhodov, Aliaksandr Siarohin, Yinghao Xu, Jian Ren, Hsin-Ying Lee, Peter Wonka, and Sergey Tulyakov. 3d generation on imagenet. In *ICLR*, 2023. 1, 2
- [40] Brandon Smart, Chuanxia Zheng, Iro Laina, and Victor Adrian Prisacariu. Splatt3r: Zero-shot gaussian splatting from uncalibrated image pairs. *arXiv preprint arXiv:2408.13912*, 2024. 3
- [41] Stanislaw Szymanowicz, Eldar Insafutdinov, Chuanxia Zheng, Dylan Campbell, Joao Henriques, Christian Rupprecht, and Andrea Vedaldi. Flash3d: Feed-forward generalisable 3d scene reconstruction from a single image. *arxiv*, 2024. 3
- [42] Stanislaw Szymanowicz, Christian Rupprecht, and Andrea Vedaldi. Splatter image: Ultra-fast single-view 3d reconstruction. In *CVPR*, 2024. 1, 2, 3
- [43] Junshu Tang, Tengfei Wang, Bo Zhang, Ting Zhang, Ran Yi, Lizhuang Ma, and Dong Chen. Make-it-3d: High-fidelity 3d creation from a single image with diffusion prior. In *ICCV*, 2023. 1, 2
- [44] Jiayang Tang, Zhaoxi Chen, Xiaokang Chen, Tengfei Wang, Gang Zeng, and Ziwei Liu. Lgm: Large multi-view gaussian model for high-resolution 3d content creation. In *ECCV*, 2024. 1, 2, 3
- [45] Vikram Voleti, Chun-Han Yao, Mark Boss, Adam Letts, David Pankratz, Dmitrii Tochilkin, Christian Laforte, Robin Rombach, and Varun Jampani. SV3D: Novel multi-view synthesis and 3D generation from a single image using latent video diffusion. In *ECCV*, 2024. 2
- [46] Junjie Wang, Jiemin Fang, Xiaopeng Zhang, Lingxi Xie, and Qi Tian. Gaussianeditor: Editing 3d gaussians delicately with text instructions. In *CVPR*, 2024. 3
- [47] Nanyang Wang, Yinda Zhang, Zhuwen Li, Yanwei Fu, Wei Liu, and Yu-Gang Jiang. Pixel2mesh: Generating 3d mesh models from single rgb images. In *ECCV*, 2018. 1
- [48] Peng Wang and Yichun Shi. Imagedream: Image-prompt multi-view diffusion for 3d generation. *arXiv preprint arXiv:2312.02201*, 2023. 1, 2
- [49] Xintao Wang, Liangbin Xie, Chao Dong, and Ying Shan. Real-esrgan: Training real-world blind super-resolution with pure synthetic data. In *ICCVW*, 2021. 2, 5
- [50] Yuxin Wang, Qianyi Wu, Guofeng Zhang, and Dan Xu. Learning 3d geometry and feature consistent gaussian splatting for object removal. In *ECCV*, 2025. 3
- [51] Zipeng Wang and Dan Xu. Pygs: Large-scale scene

- representation with pyramidal 3d gaussian splatting. *arXiv preprint arXiv:2405.16829*, 2024. 3
- [52] Zhouxia Wang, Ziyang Yuan, Xintao Wang, Yaowei Li, Tianshui Chen, Menghan Xia, Ping Luo, and Ying Shan. Motionctrl: A unified and flexible motion controller for video generation. In *ACM SIGGRAPH*, 2024. 2
- [53] Qianyi Wu, Jianmin Zheng, and Jianfei Cai. Surface reconstruction from 3d gaussian splatting via local structural hints. In *European Conference on Computer Vision*, 2024. 3
- [54] Jianfeng Xiang, Jiaolong Yang, Binbin Huang, and Xin Tong. 3d-aware image generation using 2d diffusion models. In *ICCV*, 2023. 2, 7
- [55] Chi Yan, Delin Qu, Dan Xu, Bin Zhao, Zhigang Wang, Dong Wang, and Xuelong Li. Gs-slam: Dense visual slam with 3d gaussian splatting. In *CVPR*, 2024. 3
- [56] Lihe Yang, Bingyi Kang, Zilong Huang, Xiaogang Xu, Jiashi Feng, and Hengshuang Zhao. Depth anything: Unleashing the power of large-scale unlabeled data. In *CVPR*, 2024. 3
- [57] Mingqiao Ye, Martin Danelljan, Fisher Yu, and Lei Ke. Gaussian grouping: Segment and edit anything in 3d scenes. In *ECCV*, 2025. 3
- [58] Wei Yin, Jianming Zhang, Oliver Wang, Simon Niklaus, Long Mai, Simon Chen, and Chunhua Shen. Learning to recover 3d scene shape from a single image. In *CVPR*, 2021. 3, 6
- [59] Wei Yin, Jianming Zhang, Oliver Wang, Simon Niklaus, Long Mai, Simon Chen, and Chunhua Shen. Learning to recover 3d scene shape from a single image. In *CVPR*, 2021. 1
- [60] Meng You, Zhiyu Zhu, Hui Liu, and Junhui Hou. Nvs-solver: Video diffusion model as zero-shot novel view synthesizer. *arXiv preprint arXiv:2405.15364*, 2024. 1, 2
- [61] Fisher Yu, Ari Seff, Yinda Zhang, Shuran Song, Thomas Funkhouser, and Jianxiong Xiao. Lsun: Construction of a large-scale image dataset using deep learning with humans in the loop. *arXiv preprint arXiv:1506.03365*, 2015. 6, 7, 2
- [62] Wangbo Yu, Jinbo Xing, Li Yuan, Wenbo Hu, Xiaoyu Li, Zhipeng Huang, Xiangjun Gao, Tien-Tsin Wong, Ying Shan, and Yonghong Tian. Viewcrafter: Taming video diffusion models for high-fidelity novel view synthesis. *arXiv preprint arXiv:2409.02048*, 2024. 1, 2
- [63] Zehao Yu, Torsten Sattler, and Andreas Geiger. Gaussian opacity fields: Efficient adaptive surface reconstruction in unbounded scenes. *TOG*, 2024. 3, 5, 2
- [64] Daiwei Zhang, Gengyan Li, Jiajie Li, Mickaël Bressieux, Otmar Hilliges, Marc Pollefeys, Luc Van Gool, and Xi Wang. Egogaussian: Dynamic scene understanding from egocentric video with 3d gaussian splatting. In *3DV*, 2025. 3
- [65] Kai Zhang, Sai Bi, Hao Tan, Yuanbo Xiangli, Nanxuan Zhao, Kalyan Sunkavalli, and Zexiang Xu. Gs-lrm: Large reconstruction model for 3d gaussian splatting. In *ECCV*, 2025. 1
- [66] Liu Zhiheng, Ouyang Hao, Wang Qiuyu, Cheng Ka Leong, Xiao Jie, Zhu Kai, Xue Nan, Liu Yu, Shen Yujun, and Cao Yang. Infusion: Inpainting 3d gaussians via learning depth completion from diffusion prior. *arXiv preprint arXiv:2404.11613*, 2024. 3
- [67] Yingji Zhong, Lanqing Hong, Zhenguo Li, and Dan Xu. Cvt-xrf: Contrastive in-voxel transformer for 3d consistent radiance fields from sparse inputs. In *CVPR*, 2024. 2
- [68] Hongyu Zhou, Jiahao Shao, Lu Xu, Dongfeng Bai, Weichao Qiu, Bingbing Liu, Yue Wang, Andreas Geiger, and Yiyi Liao. Hugs: Holistic urban 3d scene understanding via gaussian splatting. In *CVPR*, 2024. 3
- [69] Shangchen Zhou, Chongyi Li, Kelvin C.K Chan, and Chen Change Loy. ProPainter: Improving propagation and transformer for video inpainting. In *ICCV*, 2023. 5
- [70] Shijie Zhou, Haoran Chang, Sicheng Jiang, Zhiwen Fan, Zehao Zhu, DeJia Xu, Pradyumna Chari, Suyu You, Zhangyang Wang, and Achuta Kadambi. Feature 3dgs: Supercharging 3d gaussian splatting to enable distilled feature fields. In *CVPR*, 2024. 3
- [71] Matthias Zwicker, Hanspeter Pfister, Jeroen Van Baar, and Markus Gross. Ewa volume splatting. In *VIS*, 2001. 3

F3D-Gaus: Feed-forward 3D-aware Generation on ImageNet with Cycle-Consistent Gaussian Splatting

Supplementary Material

In this supplementary material, we provide more additional experiments in Sec. A. We also present a video demo for more qualitative results as shown in Sec. B.

A. Additional Experiments

A.1. Quantitative Fidelity Evaluation

We provide additional quantitative evaluations on three datasets: LSUN Horses [61], SDIP Dogs, and Elephants [27]. The results at a resolution of 256 are summarized in Tab. 4. Our method achieves better FID and NFS scores compared to the previous state-of-the-art approaches, indicating that our method generates more realistic images with smoother depth continuity.

Method	Dogs		Horses		Elephants	
	FID↓	NFS↑	FID↓	NFS↑	FID↓	NFS↑
EG3D [3]	9.83	11.91	2.61	13.34	3.15	2.59
EpiGRAF [37]	17.3	3.53	5.82	9.73	7.25	12.9
IVID [54]	14.7	N/A	10.2	N/A	11.0	N/A
G3DR [30]	8.37	36.89	5.64	36.2	5.30	35.6
Our F3D-Gaus	2.53	41.22	1.14	39.67	2.96	38.92

Table 4. Quantitative evaluation on the LSUN Horses [61], SDIP Dogs, and Elephants [27] datasets. Our F3D-Gaus outperforms all the previous methods on both FID and NFS.

A.2. Quantitative Efficiency Evaluation

Method	Training Time (A100 days) ↓	Inference Time (s) ↓
IVID [54]	N/A	20+128
G3DR [30]	14.5	0.9+3.6
Our F3D-Gaus	13.0	0.8+1.1

Table 5. Efficiency comparison between our method and two state-of-the-art methods. Our F3D-Gaus are tested at the resolution of 256², while the results of IVID and G3DR are at the resolution of 128².

In Tab. 5, we compare the efficiency of our method with IVID and G3DR. Training time is reported in A100 days, while the inference time is measured in seconds. Our approach reduces the training time from 14.5 A100 days (G3DR) to 13 A100 days. The “inference time” column details the time as “Time required to obtain the 3D representation + Time for rendering 128 novel views.” Benefiting from the efficiency of our pixel-aligned GS, our method achieves the fastest runtime. While G3DR’s training and inference times are close to ours, their model only supports

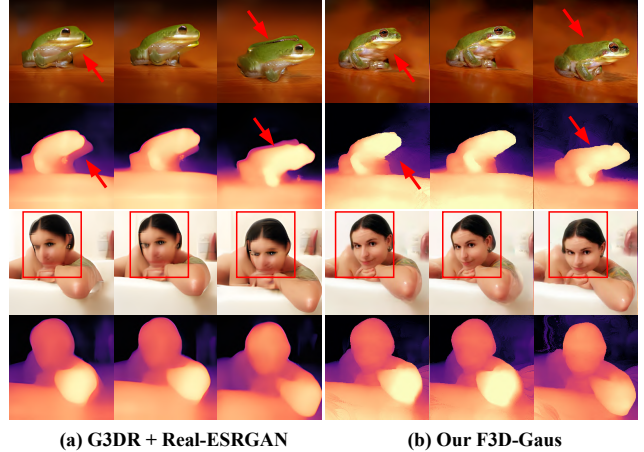


Figure 10. Qualitative comparison with G3DR [30]. We use Real-ESRGAN[49] to upsample G3DR’s 128² outputs to 256². For our F3D-Gaus, we accept 256² resolution inputs and render directly at the same 256² resolution, without requiring post-processing.

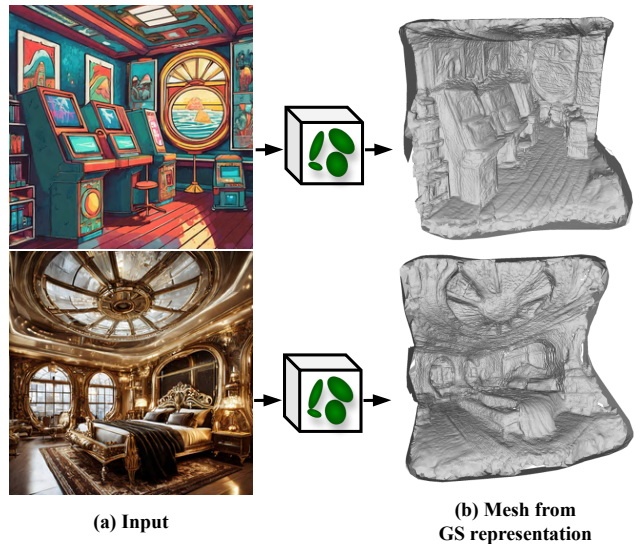


Figure 11. Visualization of the mesh extracted from the predicted 3DGS. We borrow the pipeline of GOF [63] for the mesh extraction. The mesh is directly derived from the 3DGS representation and does not rely on image-based optimization methods.

128² input images. To produce 256² outputs, G3DR requires an additional super-resolution step after inference, which introduces extra time not reflected in Tab. 5. In contrast, our method enables direct and efficient training and testing at a native 256² resolution, eliminating the need for post-processing.

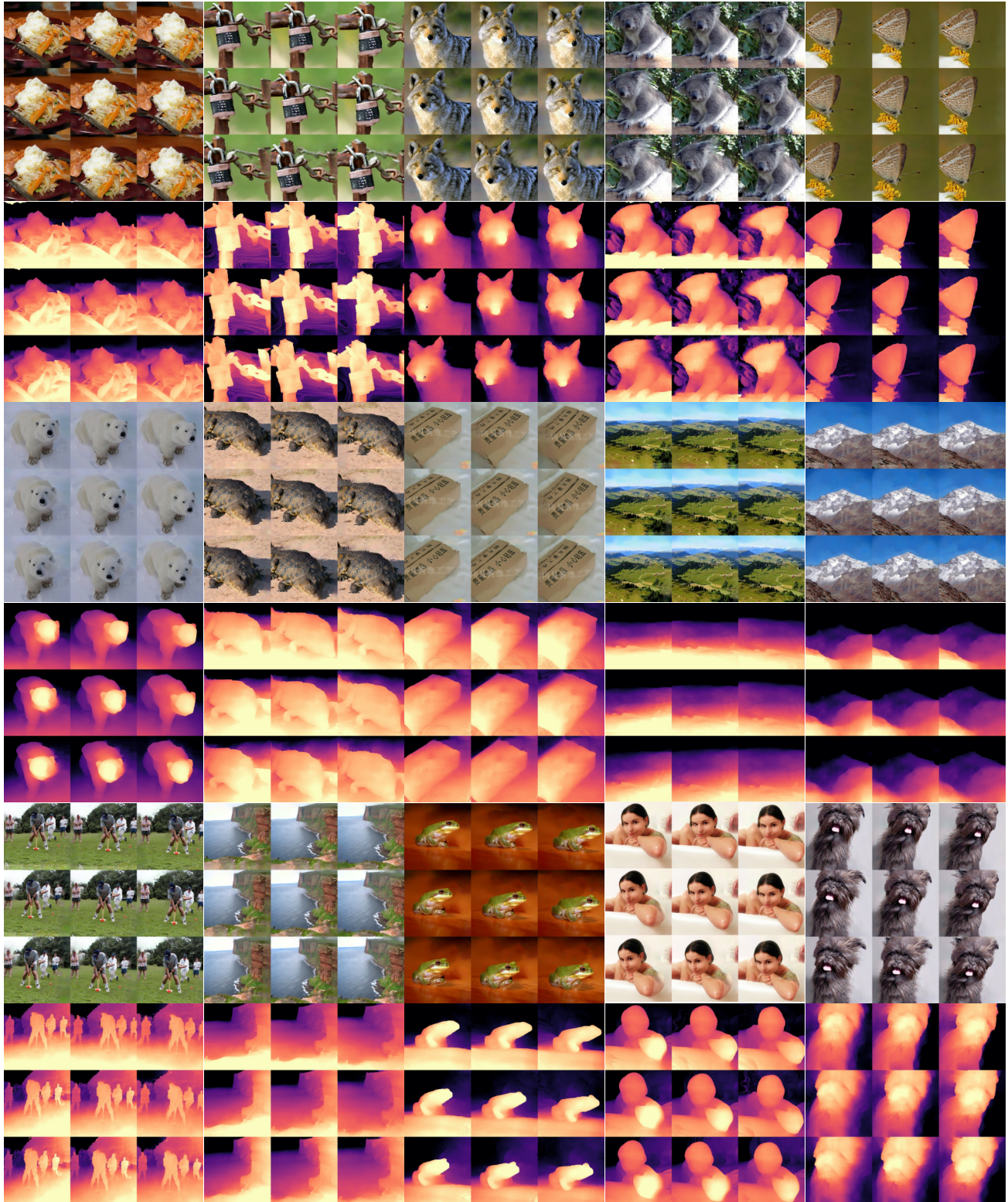


Figure 12. Additional qualitative visualization of rendered images and depth maps on the ImageNet dataset.

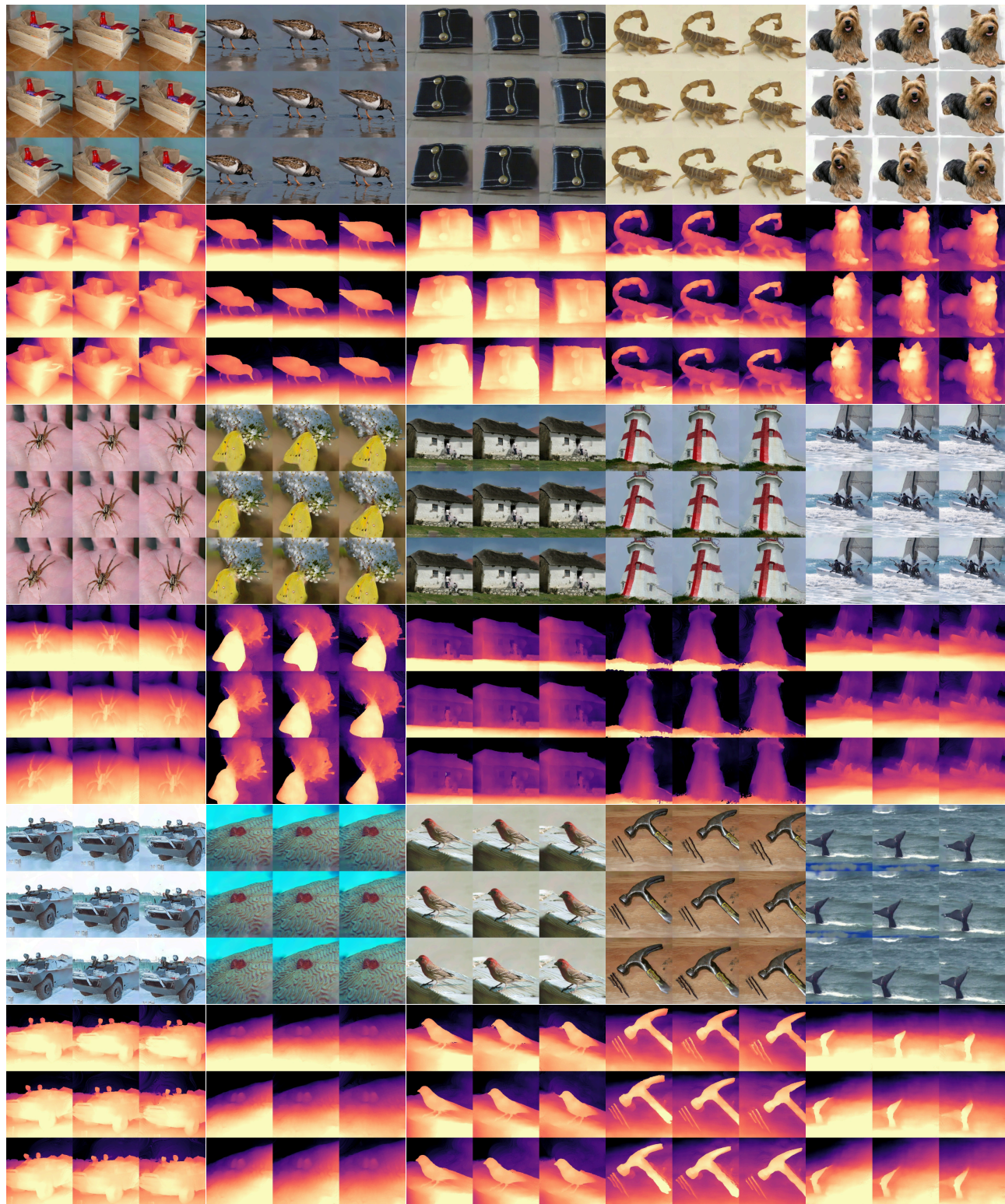


Figure 13. Another qualitative visualization of rendered images and depth maps on the ImageNet dataset.

A.3. More Qualitative Results

Fig. 10 presents a qualitative comparison between our method and G3DR. Due to the absence of the upsampling code of G3DR [30], we employ Real-ESRGAN [49], a super-resolution model known for its strong generalization on diverse images, to upsample G3DR’s 128^2 outputs to 256^2 . Although the super-resolution model can enhance sharpness in low-resolution results, it fails to address G3DR’s inherent issues, such as multi-head artifacts and lack of fine details. The red arrows and boxes in Fig. 10 highlight that our approach achieves better multi-view consistency and preserves more intricate details. In Fig. 12 and Fig. 13, we provide additional novel view synthesis results on the ImageNet dataset at the resolution of 256^2 . These qualitative results highlight that our method consistently produces images and depth across a diverse range of categories.

A.4. Mesh Extraction

Fig. 11 shows the results of mesh extraction from the predicted 3DGS. Our F3D-Gaus renders depth maps as GOF [63] for supervision. Thus, after we get the predicted 3DGS from a single image via F3D-Gaus, we could generate meshes utilizing GOF’s mesh extraction method (tetrahedral grid generation combined with binary search). Fig. 11 demonstrates the capability of our method to predict mesh from a single image via a geometry-driven pipeline leveraging 3DGS. Please note that the mesh is directly derived from the 3DGS representation and does not rely on image-based optimization methods.

A.5. Ablation on Depth Estimation

Our method currently relies on depth input, but it is technically feasible to modify the U-Net backbone to predict the depth map simultaneously. This modification would enable our method to function solely with image input while maintaining its existing capabilities. To explore this, we experimented with extending the U-Net to output an additional channel for pseudo-depth map regression, while optimizing the total loss described in the main text. The quantitative results are shown in Tab. 6. The results indicate that when the U-Net is tasked with predicting the depth map, both image metrics (FID, IS) and depth metrics (Depth Accuracy, NFS) degrade. Although the FID and IS scores remain strong compared to 3D-aware methods, the depth accuracy significantly declines. This suggests that the regressed depth map is inaccurate, and incorporating depth prediction as an additional optimization objective disrupts the learning process for image generation. We attribute this performance decline to the limitations of the current U-Net architecture, which is not specifically designed for depth map regression. Additionally, balancing multiple optimization objectives may require more sophisticated strategies. Reducing reliance on

Variants (128x)	FID ↓	IS ↑	Depth Acc ↓	NFS ↑
F3D-Gaus	1.2	202.8	0.16	40.5
F3D-Gaus w/ predicted depth	1.7	195.0	0.33	36.6

Table 6. **Comparison experiment with predicting depth simultaneously.** When the U-Net is tasked with predicting the depth map simultaneously, both image metrics (FID, IS) and depth metrics (Depth Accuracy, NFS) degrade.

depth input remains a key focus for our future work.

B. Video Demo

As a supplement to Sec. A.3, we have included a video demo to showcase the quantitative results in a video format. Please check our [project page](#) for more details. As shown in Fig.10, we use Real-ESRGAN [49] to upsample 128^2 outputs of G3DR [30] to 256^2 .